Research Article | DOI: 10.5281/zenodo.15700915
www.jnanosam.com

NANOSAM
Journal of NanoScience in Advanced Materials

Near-Infrared Light-Activated Antibacterial Efficiency of Flower-like MoS_2 with Varying Concentrations

Ahmed Al-Sarori[1], Abdurrahman Mustafa[1], and Burak Kıvrak[2,#]

In this study, flower-like MoS_2 particles with a 2H crystal structure were synthesized via a hydrothermal method to evaluate their photothermal efficiency and antibacterial activity against Staphylococcus aureus and Escherichia coli. The structural, morphological, optical, and photothermal properties of the synthesized MoS_2 were comprehensively characterized. X-ray diffraction analysis confirmed that MoS_2 formed as 2H with no detectable impurities, while electron microscopy revealed a flower-like morphology. Optical characterization in the 400–1000 nm wavelength range indicated a direct band gap of approximately 1.9 eV. Photothermal performance was investigated using 808 nm laser irradiation in combination with thermal imaging, which demonstrated a maximum temperature increase of 46 °C at a concentration of 1000 μg mL^{-1} and uniform heat distribution throughout the solution. Furthermore, antibacterial tests using agar plates showed that the antibacterial activity of MoS_2 was more pronounced at lower concentrations for both bacterial species, suggesting a concentration-dependent effect.

1. Introduction

As time progresses, bacterial infections are becoming increasingly severe, contributing to rising mortality rates worldwide [1]. Besides, the widespread and excessive use of antibiotic has led to the development of resistance in bacteria, complicating their eradication and creating significant public health challenges [1-3]. Recent advancements in nanotechnology have facilitated the development of novel antibacterial strategies and materials to fight bacterial infections effectively [1, 4-6]. It has been proven by many the studies that diverse stimulations like, light and magnetic field, materials show antibacterial effect and hinders effect of bacteria [1, 7, 8]. In particular, the light stimulation, especially near infrared (NIR) irritation is the best choice in different aspects [1, 9]. Materials interacting with NIR (700–1000 nm) light creating heat to eradicate pathogens or diseased cells, has emerged as a non-invasive and efficient treatment modality, particularly in biomedical applications [9-13].

Transition metal dichalcogenides (TMDs) have emerged as promising candidates for antibacterial applications due to their unique properties, including biocompatibility, tunable structural parameters, cost-effectiveness, environmental friendliness, and favourable physicochemical characteristics [5, 14-16]. Among TMDs, molybdenum disulfide (MoS_2) emerges as a widely utilized material in diverse applications such as hydrogen evolution, photovoltaics, supercapacitors, microwave absorption, sensing, and drug delivery [17-23]. Within a single layer of MoS_2, molybdenum (Mo) and sulphur (S) atoms form covalent bonds, whereas weak van der Waals forces connect neighbouring layers [24, 25]. MoS_2 can crystallize in three distinct polymorphs: 2H (a thermodynamically stable semiconducting phase with hexagonal symmetry), 1T (a metastable semi metallic phase with trigonal symmetry), and 3R (semiconducting phase with rhombohedral symmetry) [26, 27]. The coordination of Mo and S atoms varies among these phases: both 2H and 3R exhibit trigonal prismatic coordination, while 1T adopts an octahedral configuration. This difference in coordination significantly influences the electronic structure of MoS_2, resulting in semiconducting behaviour in the 2H and 3R phases and semi metallic behaviour in the 1T phase [28]. Moreover, the bandgap of 2H MoS_2 is highly

[1]Department of Chemical Engineering, Konya Technical University, 42250, Konya, TÜRKİYE [2]Department of Metallurgical and Materials Science Engineering, Konya Technical University, 42250, Konya, TÜRKİYE

#Corresponding author: bkivrak@ktun.edu.tr

Keywords: Photothermal activity; Flower-like MoS_2; Antibacterial particles; NIR irridation

Received: 21 April 2025 | Accepted: 19 May 2025 | Published online: 26 June 2025

dependent on the number of layers. As the layer thickness decreases, the bandgap increases from approximately 1.2 eV to 1.9 eV, accompanied by a transition from indirect to direct bandgap characteristics [24, 29, 30]. In addition to its electronic and optical properties, MoS_2 demonstrates strong NIR absorption, low toxicity, and excellent photothermal conversion efficiency, making it a promising candidate for photothermal antibacterial applications [14, 31-35]. It has been shown that MoS_2 induces membrane stress and generates reactive oxygen species (ROS), further enhancing its contributing to its potential antibacterial properties [14].

Herein, flower-like MoS_2 particles were synthesized via hydrothermal synthesis, and their structural, morphological, optical, and photothermal properties were characterized. Additionally, the NIR-induced antibacterial activity of MoS_2 was evaluated against *Staphylococcus aureus* (*S. aureus*) and *Escherichia coli* (*E. coli*). The results indicate that MoS_2 crystallizes in the 2H phase and forms a flower-like morphology. Optical characterization confirmed a direct bandgap of 1.9 eV. Photothermal experiments revealed a maximum temperature of 46°C at a concentration of 1000 µg mL^{-1}, with thermal camera imaging indicating uniform heating in solution. Notably, higher antibacterial efficacy was achieved at lower MoS_2 concentrations.

2. Results and Discussion

2.1. Structural characteristics

Figure 1 illustrates the diffraction patterns of the synthesized samples. The black vertical lines at the bottom of the diffraction data correspond to the JCPDS card for trigonal prismatic (2H) MoS_2 with a space group P63/mmc (Hexagonal crystal system a: 3.1612 Å, b: 3.1612 Å and c: 12.2985 Å, JCPDS: 00-037-1492). It can be seen from the figure that the diffraction pattern of the synthesized samples aligns closely with reference card data. The primary peak of 2H MoS_2, associated with the (002) plane, appears at 2θ = 14.01°, consistent with literature values [38-40]. Additional peaks observed at 2θ = 32.73°, 36.32°, and 57.90° correspond to the (100), (102), and (110) planes, respectively. No impurities or secondary phases were detected in the diffraction data.

2.2. Morphological characteristics

The morphological characteristics of flower-like MoS_2 particles are shown in Fig. 2. The images reveal that MoS_2 forms flower-like structures, resulting from the assembly of nanosheets. This morphology emerges through a process involving nucleation and growth of nanosheets, followed by their self-organization into a preferred orientation [41, 42]. The average particle size was determined using the X'Pert HighScore software, analysing 100 particles with a lognormal distribution fit. The calculations yielded an average particle size of 2.53 µm. Despite challenges in size determination due to particle agglomeration, measurements were performed by selecting particles as indicated by pink arrows in Fig. 2(a).

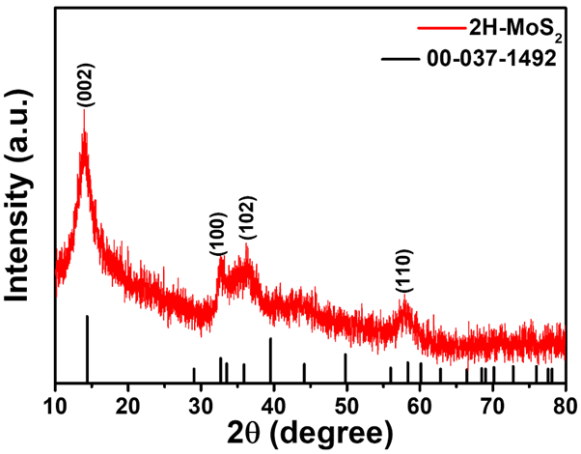

Figure 1. XRD pattern of synthesized samples.

2.3. Optical properties

The optical properties of the synthesized MoS_2 samples were examined using UV-Vis spectroscopy across the 400–1000 nm wavelength range, as shown in Fig. 3. The absorption spectra display a broad absorption band. Typically, MoS_2 exhibits characteristic peaks at ~350, 440, 600, and 650 nm [43-45]. In this study, however, these four characteristic peaks are absent, likely due to the excitonic properties of MoS_2 [44, 46]. Additionally, Tauc plots were generated using the following equation (Eq. 1),

$$(\alpha h\nu)^{1/n} = A(h\nu - E_g) \quad (1)$$

where α is the absorption coefficient, $h\nu$ represents the incident photon energy, A is energy independent constant, and n is an exponent determined by the type of electronic transition (n = 1/2 for direct transitions, n = 2 for indirect transitions). From the Tauc plots, the direct bandgap was calculated to be 1.9 eV, and the indirect bandgap was 1.4 eV, both of which align well with literature values [47, 48].

2.4. Photothermal properties

The photothermal characteristics of MoS_2 particles were first studied under 808 nm NIR irradiation at a power density of 2.5 W cm^{-2}, across concentrations of 50, 100, 250, 500, and 1000 µg mL^{-1}, as depicted in Fig. 4(a). Upon light exposure,

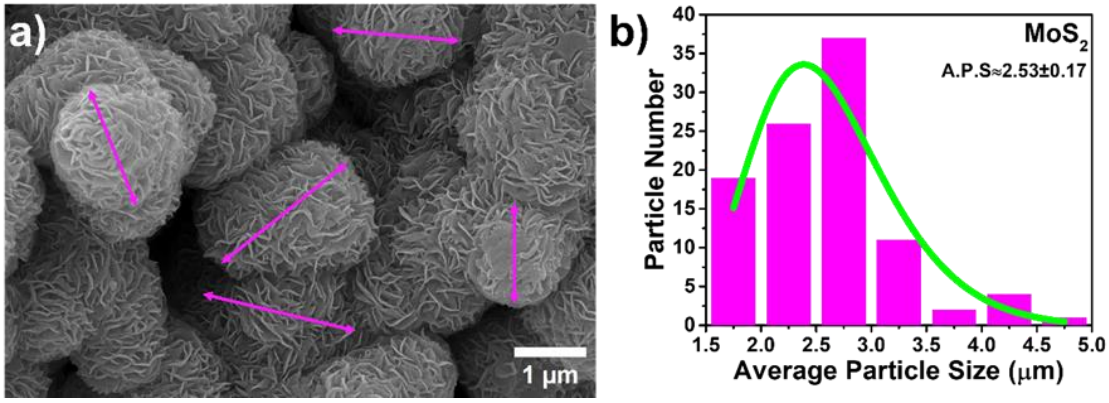

Figure 2. Morphological features of flower like MoS_2 particles, (a) SEM image and (b) Particle size distribution graph.

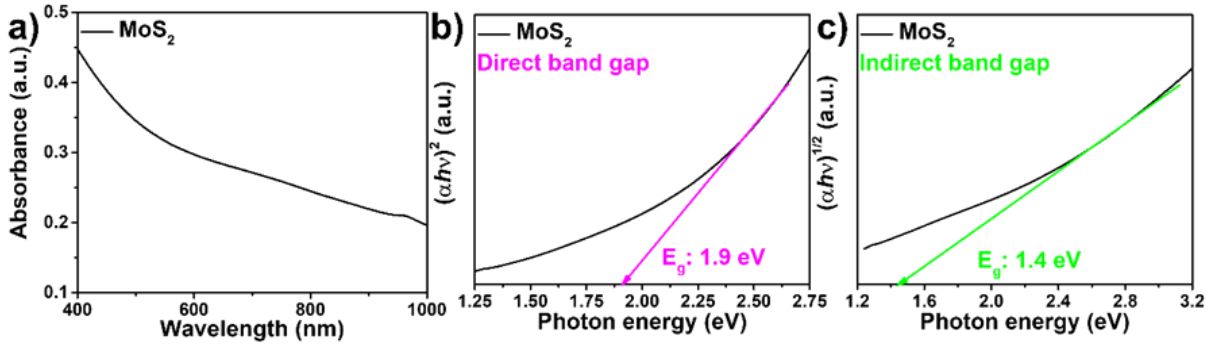

Figure 3. Optical properties of MoS_2, (a) absorbance spectrum and (b-c) Tauc plots.

all samples show a rapid temperature increase within the initial 0–100 seconds, after which the temperature increase rate diminishes. The figure also indicates that photothermal activity increases with increasing particle concentration, likely due to the greater number of active sites available for heat generation. The maximum temperature, recorded at 46°C, corresponds to the 1000 μg mL^{-1} concentration. A thermal camera image or contour plot, in Fig. 4(b), confirms the temperature increase over the time period.

Subsequently, the sample exhibiting superior performance (1000 μg mL^{-1}) was further analyzed to explore the dependence of photothermal activity on power density. Fig. 4(c) illustrates the response at power density levels of 0.5, 1.0, 2.0, and 2.5 W cm^{-2}, confirming that maximum achievable temperature increases with higher power density, as expected. Furthermore, the photothermal cycling behaviour of MoS_2 particles was investigated through five consecutive on/off cycles of 808 nm NIR irradiation, as shown in Fig. 5(a). Each cycle exhibited almost consistent temperatures, demonstrating the excellent photothermal stability of the MoS_2 particles. The time constant (τ) and photothermal conversion efficiency were calculated using Eq. 4 and the data illustrated in Fig 5(b). The τ and photothermal conversion efficiency values were found as 317.2 s and 55.7%, respectively.

2.5. Antibacterial activity

Figure 6 illustrates the *in vitro* antibacterial activity of the synthesized sample against *S. aureus* and *E. coli* without NIR irradiation. As can be seen from the images that there is no reduction in bacterial presence without irradiation. However, when activated by light, an antibacterial effect was observed, as shown in Fig. 7. According to the images, the incubated bacterial concentration decreased under light activation. Furthermore, The antibacterial activity (%) of MoS_2 nanoparticles as a function of concentration against *E. coli* and *S. aureus* is presented in Figs. 7(b) and 7(d). For both bacterial cultures, antibacterial activity was strongly dependent on the concentration of MoS_2. As illustrated in graphs, lower concentrations of MoS_2 resulted in higher antibacterial activity, indicating that reduced concentrations are more effective in eliminating bacteria. It can be seen from the images (see Figs. 7(a) and (c)) that material exhibit enhanced antibacterial activity against *S. aureus* and *E. coli* when concentration is decreased. This can be explained through the interplay of material properties and bacterial interactions. Generally, MoS_2 behaves as hydrophobic material and tend to aggregate in water environments [49, 50]. At higher concentrations it is believed that MoS_2 particles tend to aggregate in aqueous

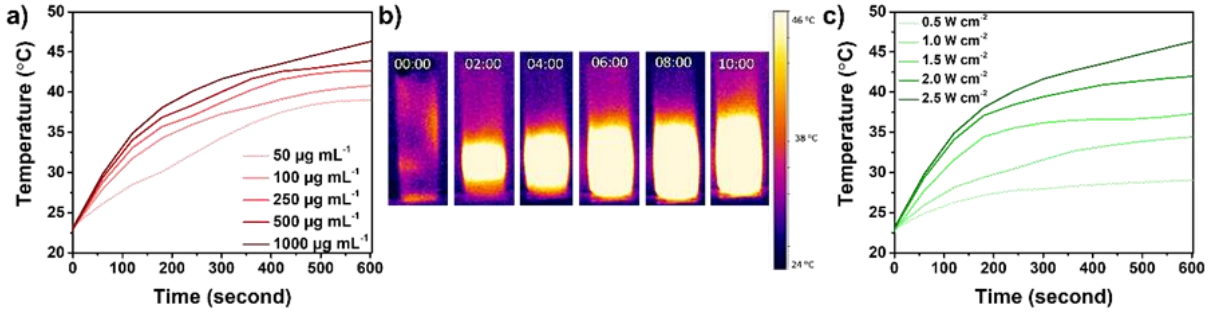

Figure 4. Photothermal response of MoS_2, a) heating curve of MoS_2 at a power density of 2.5 W cm^{-2}, across concentrations of 50, 100, 250, 500, and 1000 µg mL^{-1}, b) thermal camera image of sample heating and c) heating curve of MoS_2 (1000 µg mL^{-1}) at power density levels of 0.5, 1.0, 2.0, and 2.5 W cm^{-2}

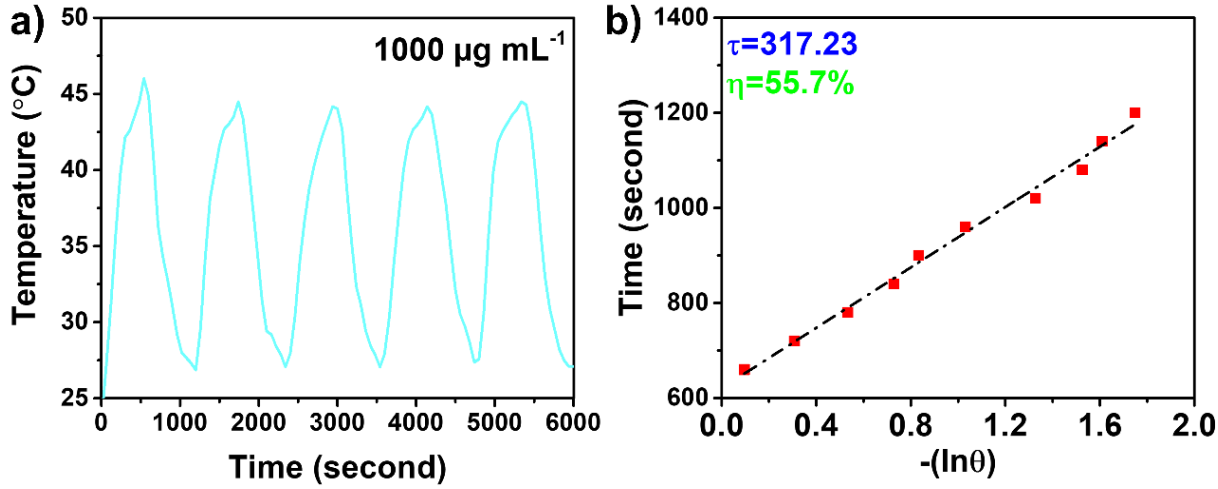

Figure 5. (a) Photothermal stability of the particles under NIR light on/off cycles (NIR power density: 2.5 W cm^{-2}, MoS_2 concentration: 1000 µg mL^{-1}) and (b) linear regression curve obtained from cooling data in distilled water.

environments, forming clusters that reduce their effective surface area. Thus, this aggregation limits direct contact with bacterial cell walls, thereby decreasing the efficiency of antibacterial mechanisms such as membrane disruption with physical interaction or localized heating NIR irradiation [14]. Conversely, at lower concentrations, the nanoparticles remain well-dispersed, maximizing their surface area and enabling more effective interactions with bacterial cells.

3. Conclusion

In summary, flower-like MoS_2 particles with a 2H phase were successfully synthesized via a hydrothermal approach and demonstrated promising photothermal and antibacterial properties. The material exhibited strong NIR absorption with a direct band gap of 1.9 eV and achieved a significant temperature increase under 808 nm laser irradiation, indicating efficient photothermal conversion. Moreover, MoS_2 displayed effective antibacterial activity against both *S. aureus* and *E. coli*, particularly at lower concentrations. These findings highlight the potential of MoS_2 as a biocompatible and efficient photothermal agent for antibacterial applications, paving the way for its further development in biomedical and antimicrobial technologies.

Method

Materials

Sodium molybdate dihydrate ($Na_2MoO_4.2H_2O$, Sigma-Aldrich, ≥99.0%), thiourea (CH_4N_2S, Alfa Aesar 99%), oxalic acid ($C_2H_2O_4.2H_2O$, ≥99.0%), Deionized (DI) water and ethyl alcohol (EA, Tekkim, 96%) were used for material synthesis and cleaning/washing purposes. Mueller-Hinton broth and Mueller-Hinton agar were purchased from Merck. Phosphate buffer saline (PBS) was purchased from Sigma-Aldrich.

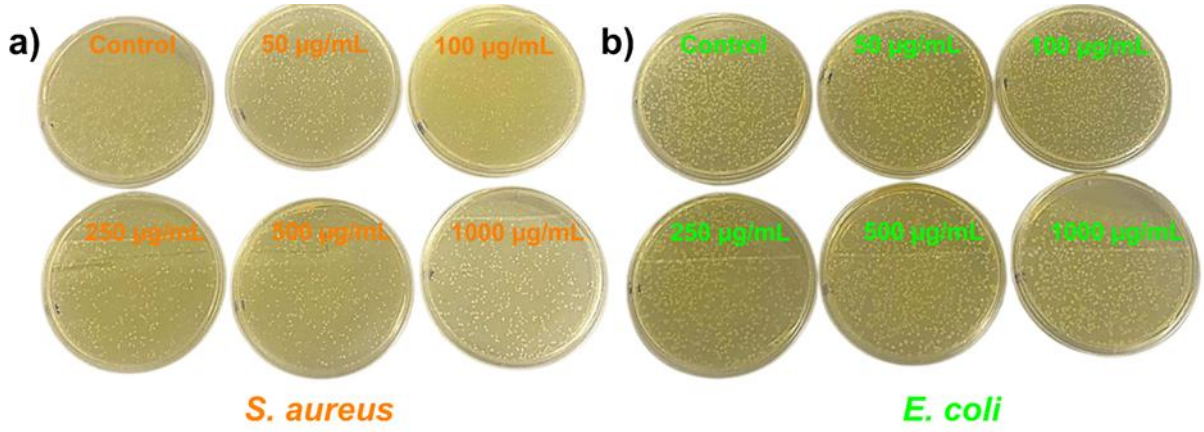

Figure 6. Spread agar plates belonging to (a) S. aureus and (b) E. coli bacteria without NIR irridation (the number 1000, 500, 250, 100 and 50 refers to MoS_2 concentration as µg mL^{-1}).

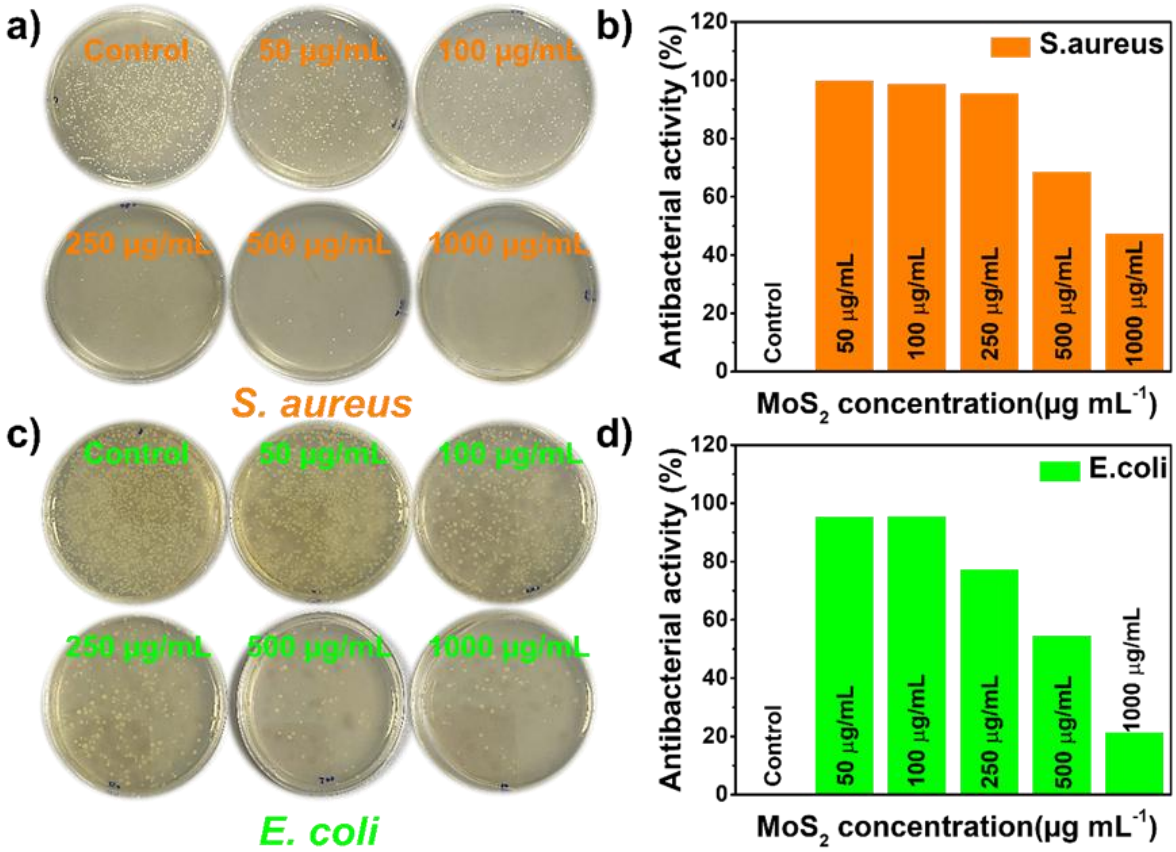

Figure 7. Antibacterial activity of MoS_2 against S. aureus and E. coli bacteria with NIR irritation, (a) Spread agar plates belonging to S. aureus, (b) Antibacterial activity of MoS_2 as a function of concentration against S. aureus, (c) Spread agar plates belonging to E. coli and (d) Antibacterial activity of MoS_2 as a function of concentration against E. coli.

Synthesis of flower-like MoS_2

Hydrothermal synthesis was employed to produce flower-like MoS_2 particles, with the process illustrated in Fig.8. To prepare the solution, Na_2MoO_4 was first dissolved in DI water and mixed with magnetic stirrer for 10 min. Next, thiourea was added and the solution left for mixing for another 10 min. Oxalic acid was subsequently introduced, followed by 1 h of mixing. The solution was then sealed in a Teflon-lined autoclave and heated at 200 °C for 20 h. The resulting black powders were washed several times with DI water and ethanol and dried at 80 °C in an oven under ambient conditions for 8 h.

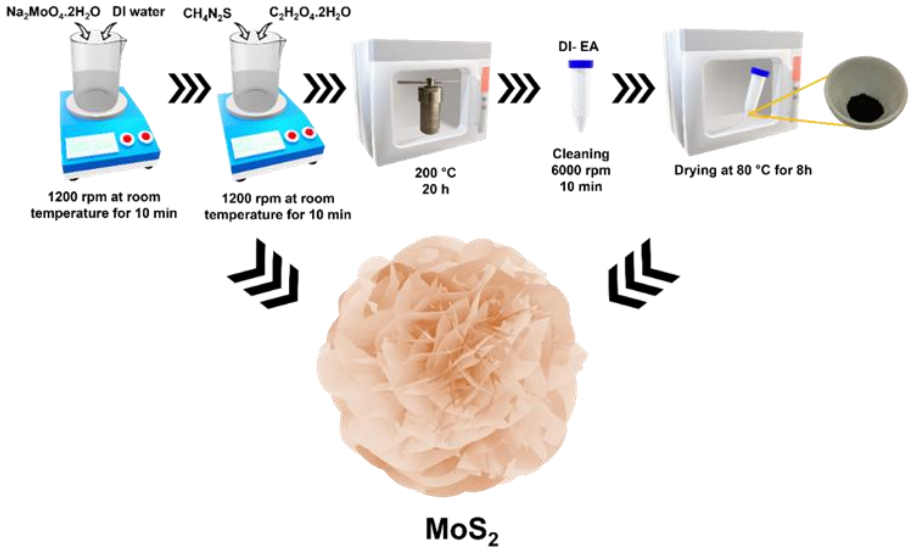

Figure 8. Schematic illustration of the synthesis procedures of flower-like MoS_2.

Photothermal activity experiments

The photothermal properties of MoS_2 particles were investigated under 808 nm NIR light irradiation for 10 min, varying the NIR power density and particle concentration. Antibacterial efficiency was tested against *S. aureus* and *E. coli* using the spread plate technique under optimized conditions. MoS_2 suspensions at concentrations of 50, 100, 250, 500, and 1000 μg mL^{-1} were sonicated in distilled water for 1 h. Then sonicated particles were transferred to quartz cuvettes for exposure to 808 nm NIR light at power densities levels of 0.5, 1.0, 1.5, 2.0, and 2.5 W cm^{-2} for 10 min. Real-time temperature changes in the suspensions were monitored using an Optris Xi 400 infrared camera, with corresponding thermal images captured. After 10 min of heating, the NIR source was turned off, and the cooling phase was recorded for an additional 10 min. In order to assess the photothermal stability of synthesized samples, temperature variation profiles were collected across five cycles. The photothermal conversion efficiency (η) was determined using Eq. 2,

$$\eta = \frac{h\,A\,\Delta t_{max} - Q_s}{I\left(1-10^{A_\lambda}\right)} \quad (2)$$

where h represents the heat transfer coefficient, A denotes the heated surface area of the cuvette, ΔT_{max} is the maximum temperature difference at steady state, Q_s refers the heat of the control solution, I indicates the NIR laser power, and A_λ is the absorbance of the materials at 808 nm [36]. The hA value was calculated using Eqs. 3-5, with the time constant τ derived from the $t - \ln\theta$ curve. Here, T_{amb} and T_{max} represent the ambient and maximum temperatures, respectively, t is time, θ is a dimensionless parameter, and m and C_p denote the mass and heat capacity of the dispersion solution, respectively [37].

$$\theta = \frac{T - T_{amb}}{T_{max} - T_{amb}} \quad (3)$$

$$t = -\tau ln\theta \quad (4)$$

$$hA = \frac{mC_p}{\tau} \quad (5)$$

Characterization techniques

The structural parameters of samples were specified using X-ray diffractometer with Cu-K_α (Cu-$K\alpha$ = 1.5406 Å, range: 5-80° with a step size of 0.01°) radiation provided by the Rigaku-MiniFlex600. The morphological features and chemical state of elements in samples were specified by scanning electroscope (SEM, FEI-Quanta 650D FEG) equipped. The UV–vis-NIR spectrophotometer (Shimadzu UV-1800) in the wavelength range of 400–1000 nm was used to investigate optical properties of synthesized materials. Real-time temperature changes in the suspensions were monitored using an Optris Xi 400 infrared camera.

Acknowledgements

The authors express their gratitude to Dr. Gülcihan Güzel Kaya, Dr. Hasan Akyıldız and Dr. İsmail Cihan Kaya for valuable assistance during measurements and for providing laboratory facilities.

Authors' contributions:

AA: Performed photothermal experiments/data collection, data analysis, and interpretation, drafted the paper. **AM:** Performed antibacterial experiments/data collection, data analysis, and interpretation, drafted the paper. **BK:** Synthesized materials, performed experiments/data collection, data analysis, and interpretation, drafted the paper, and provided grammatical revisions to the manuscript, provided revisions to scientific content of the manuscript

Data Availability Statement

The data that support the findings of this study are available from the corresponding author upon reasonable request.

Declaration of Ethical Standards

The author(s) of this article declare that the materials and methods used in this study do not require ethical committee permission and/or legal-special permission.

Declaration of generative AI and AI-assisted technologies in the writing process

During the preparation of this work the author used Grok 3 to correct the grammatical faults in the manuscript. After using this tool/service, the author reviewed and edited the content as needed and takes full responsibility for the content of the published article.

Conflict of Interest

There is no conflict of interest in this study.

References

[1] Han, Q., Lau, J.W., Do, T.C., Zhang, Z., Xing, B., Near-Infrared Light Brightens Bacterial Disinfection: Recent Progress and Perspectives, ACS Applied Bio Materials **4**, 3937-61 (2021).

[2] Liu, L., Wu, W., Fang, Y., Liu, H., Chen, F., Zhang, M., et al., Functionalized MoS2 Nanoflowers with Excellent Near-Infrared Photothermal Activities for Scavenging of Antibiotic Resistant Bacteria, Nanomaterials **11**, 2829 (2021).

[3] Zumla, A., Nahid, P., Cole, S.T., Advances in the development of new tuberculosis drugs and treatment regimens, Nature Reviews Drug Discovery **12**, 388-404 (2013).

[4] Dediu, V., Ghitman, J., Gradisteanu Pircalabioru, G., Chan, K.H., Iliescu, F.S., Iliescu, C., Trends in Photothermal Nanostructures for Antimicrobial Applications, International Journal of Molecular Sciences **24**, 9375 (2023).

[5] Tang, Y., Qin, Z., Yin, S., Sun, H., Transition metal oxide and chalcogenide-based nanomaterials for antibacterial activities: an overview, Nanoscale **13**, 6373-88 (2021).

[6] Velema, W.A., van der Berg, J.P., Hansen, M.J., Szymanski, W., Driessen, A.J.M., Feringa, B.L., Optical control of antibacterial activity, Nature Chemistry **5**, 924-8 (2013).

[7] Wang, Y., Yang, Y., Shi, Y., Song, H., Yu, C., Antibiotic-Free Antibacterial Strategies Enabled by Nanomaterials: Progress and Perspectives, Adv Mater **32**, 1904106 (2020).

[8] Yang, J., Wang, C., Liu, X., Yin, Y., Ma, Y.-H., Gao, Y., et al., Gallium–Carbenicillin Framework Coated Defect-Rich Hollow TiO2 as a Photocatalyzed Oxidative Stress Amplifier against Complex Infections, Adv Funct Mater **30**, 2004861 (2020).

[9] Cai, Y., Wei, Z., Song, C., Tang, C., Han, W., Dong, X., Optical nano-agents in the second near-infrared window for biomedical applications, Chem Soc Rev **48**, 22-37 (2019).

[10] Feng, Y., Liu, L., Zhang, J., Aslan, H., Dong, M., Photoactive antimicrobial nanomaterials, Journal of Materials Chemistry B **5**, 8631-52 (2017).

[11] Li, W., Dong, K., Wang, H., Zhang, P., Sang, Y., Ren, J., et al., Remote and reversible control of in vivo bacteria clustering by NIR-driven multivalent upconverting nanosystems, Biomaterials **217**, 119310 (2019).

[12] Dong, K., Ju, E., Gao, N., Wang, Z., Ren, J., Qu, X., Synergistic eradication of antibiotic-resistant bacteria based biofilms in vivo using a NIR-sensitive nanoplatform, Chem Commun **52**, 5312-5 (2016).

[13] Zhang, A., Li, A., Zhao, W., Liu, J., Recent Advances in Functional Polymer Decorated Two-Dimensional Transition-Metal Dichalcogenides Nanomaterials for Chemo-Photothermal Therapy, Chemistry – A European Journal **24**, 4215-27 (2018).

[14] Yang, X., Li, J., Liang, T., Ma, C., Zhang, Y., Chen, H., et al., Antibacterial activity of two-dimensional MoS2 sheets, Nanoscale **6**, 10126-33 (2014).

[15] Wang, Z., Zhu, W., Qiu, Y., Yi, X., von dem Bussche, A., Kane, A., et al., Biological and environmental interactions of emerging two-dimensional nanomaterials, Chem Soc Rev **45**, 1750-80 (2016).

[16] Mondal, A., De, M., Exfoliation, functionalization and antibacterial activity of transition metal dichalcogenides, Tungsten **6**, 1-16 (2024).

[17] Ahn, E., Kim, B.S., Multidimensional Thin Film Hybrid Electrodes with MoS2 Multilayer for Electrocatalytic Hydrogen Evolution Reaction, ACS Appl Mater Interfaces **9**, 8688-95 (2017).

[18] Lim, Y.R., Song, W., Han, J.K., Lee, Y.B., Kim, S.J., Myung, S., et al., Wafer-Scale, Homogeneous MoS2 Layers on Plastic Substrates for Flexible Visible-Light Photodetectors, Adv Mater **28**, 5025-30 (2016).

[19] Acerce, M., Voiry, D., Chhowalla, M., Metallic 1T phase MoS2 nanosheets as supercapacitor electrode materials, Nat Nanotechnol **10**, 313-8 (2015).

[20] Kıvrak, B., Akyıldız, H., Akgöl, O., Karaaslan, M., Akyol, M., Polyaniline-Functionalized Nanosized Cobalt Ferrite-Decorated MoS2 Composites for Broadband Electromagnetic Wave Absorption, ACS Applied Electronic Materials **6**, 8211-25 (2024).

[**21]** Chaudhary, N., Khanuja, M., Abid, Islam, S.S., Hydrothermal synthesis of MoS2 nanosheets for multiple wavelength optical sensing applications, Sens Actuator A Phys **277**, 190-8 (2018).

[22] Ghosh, S., Lai, J.-Y., An insight into the dual role of MoS2-based nanocarriers in anticancer drug delivery and therapy, Acta Biomaterialia **179**, 36-60 (2024).

[23] Singh, E., Singh, P., Kim, K.S., Yeom, G.Y., Nalwa, H.S., Flexible Molybdenum Disulfide (MoS2) Atomic Layers for Wearable

Electronics and Optoelectronics, ACS App Mater Interfaces **11**, 11061-105 (2019).

[24] Radisavljevic, B., Radenovic, A., Brivio, J., Giacometti, V., Kis, A., Single-layer MoS2 transistors, Nat Nanotechnol **6**, 147-50 (2011).

[25] Kumar, A., Ahluwalia, P.K., Semiconductor to metal transition in bilayer transition metals dichalcogenides MX2 (M = Mo, W; X = S, Se, Te), Modell Simul Mater Sci Eng **21**, 065015 (2013).

[26] Zhao, W., Pan, J., Fang, Y., Che, X., Wang, D., Bu, K., et al., Metastable MoS2: Crystal Structure, Electronic Band Structure, Synthetic Approach and Intriguing Physical Properties, Chemistry – A European Journal **24**, 15942-54 (2018).

[27] Feng, G., Wei, A., Zhao, Y., Liu, J., Synthesis of flower-like MoS2 nanosheets microspheres by hydrothermal method, J Mater Sci Mater Electron **26**, 8160-6 (2015).

[28] Strachan, J., Masters, A.F., Maschmeyer, T., 3R-MoS2 in Review: History, Status, and Outlook, ACS Applied Energy Materials **4**, 7405-18 (2021).

[29] Jin, W., Yeh, P.-C., Zaki, N., Zhang, D., Sadowski, J.T., Al-Mahboob, A., et al., Direct Measurement of the Thickness-Dependent Electronic Band Structure of MoS2 Using Angle-Resolved Photoemission Spectroscopy, Phys Rev Lett **111**, 106801 (2013).

[30] Cheiwchanchamnangij, T., Lambrecht, W.R.L., Quasiparticle band structure calculation of monolayer, bilayer, and bulk MoS2, Physical Review B **85**, 205302 (2012).

[31] Yin, W., Yu, J., Lv, F., Yan, L., Zheng, L.R., Gu, Z., et al., Functionalized Nano-MoS2 with Peroxidase Catalytic and Near-Infrared Photothermal Activities for Safe and Synergetic Wound Antibacterial Applications, ACS Nano **10**, 11000-11 (2016).

[32] Gao, Q., Zhang, X., Yin, W., Ma, D., Xie, C., Zheng, L., et al., Functionalized MoS2 Nanovehicle with Near-Infrared Laser-Mediated Nitric Oxide Release and Photothermal Activities for Advanced Bacteria-Infected Wound Therapy, Small **14**, 1802290 (2018).

[33] Chng, E.L.K., Sofer, Z., Pumera, M., MoS2 exhibits stronger toxicity with increased exfoliation, Nanoscale **6**, 14412-8 (2014).

[34] Shah, P., Narayanan, T.N., Li, C.-Z., Alwarappan, S., Probing the biocompatibility of MoS2 nanosheets by cytotoxicity assay and electrical impedance spectroscopy, Nanotechnology **26**, 315102 (2015).

[35] Yin, W., Yan, L., Yu, J., Tian, G., Zhou, L., Zheng, X., et al., High-Throughput Synthesis of Single-Layer MoS2 Nanosheets as a Near-Infrared Photothermal-Triggered Drug Delivery for Effective Cancer Therapy, ACS Nano **8**, 6922-33 (2014).

[36] Getiren, B., Çıplak, Z., Gökalp, C., Yıldız, N., Novel approach in synthesizing ternary GO-Fe3O4-PPy nanocomposites for high Photothermal performance, J Appl Polym Sci **137**, 48837 (2020).

[37] AlSarori, A., Mustafa, A., Akyıldız, H., Kaya, I.C., Kaya, G.G., Non-Stoichiometric FeS2 nanoparticles as antibacterial agents with combined photothermal and photodynamic effect, Journal of Photochemistry and Photobiology A: Chemistry **462**, 116260 (2025).

[38] Mishra, S., Maurya, P.K., Mishra, A.K., 2H–MoS2 nanoflowers based high energy density solid state supercapacitor, Materials Chemistry and Physics **255**, 123551 (2020).

[39] Rajapriya, A., Keerthana, S., Viswanathan, C., Ponpandian, N., Direct growth of MoS2 hierarchical nanoflowers on electrospun carbon nanofibers as an electrode material for high-performance supercapacitors, J Alloys Compd **859**, 157771 (2021).

[40] Kıvrak, B., Akyol, M., Ekicibil, A., Investigation of structural and magnetic characteristic of pure and M-doped (M: Fe and Cu) MoS2 thin films, J Mater Sci Mater Electron **33**, 16574-85 (2022).

[41] Zheng, X., Zhu, Y., Sun, Y., Jiao, Q., Hydrothermal synthesis of MoS2 with different morphology and its performance in thermal battery, Journal of Power Sources **395**, 318-27 (2018).

[42] Sun, Z., Liao, T., Dou, Y., Hwang, S.M., Park, M.-S., Jiang, L., et al., Generalized self-assembly of scalable two-dimensional transition metal oxide nanosheets, Nature Communications **5**, 3813 (2014).

[43] Li, B., Jiang, L., Li, X., Ran, P., Zuo, P., Wang, A., et al., Preparation of Monolayer MoS2 Quantum Dots using Temporally Shaped Femtosecond Laser Ablation of Bulk MoS2 Targets in Water, Scientific Reports **7**, 11182 (2017).

[44] Xu, S., Li, D., Wu, P., One-Pot, Facile, and Versatile Synthesis of Monolayer MoS2/WS2 Quantum Dots as Bioimaging Probes and Efficient Electrocatalysts for Hydrogen Evolution Reaction, Adv Funct Mater **25**, 1127-36 (2015).

[45] Wilcoxon, J.P., Newcomer, P.P., Samara, G.A., Synthesis and optical properties of MoS2 and isomorphous nanoclusters in the quantum confinement regime, Journal of Applied Physics **81**, 7934-44 (1997).

[46] Wilcoxon, J.P., Samara, G.A., Strong quantum-size effects in a layered semiconductor: MoS2 nanoclusters, Physical Review B **51**, 7299-302 (1995).

[47] Chen, L., Hsieh, S.-L., Kuo, C.-H., Hsieh, S., Chen, W.-H., Chen, C.-W., et al., Novel MoS2 quantum dots as a highly efficient visible-light driven photocatalyst in water remediation, RSC Advances **10**, 31794-9 (2020).

[48] Drozdowska, K., Smulko, J., Czubek, J., Rumyantsev, S., Kwiatkowski, A., UV-assisted fluctuation-enhanced gas sensing by ink-printed MoS2 devices, Scientific Reports **14**, 22172 (2024).

[49] Roy, S., Mondal, A., Yadav, V., Sarkar, A., Banerjee, R., Sanpui, P., et al., Mechanistic Insight into the Antibacterial Activity of Chitosan Exfoliated MoS2 Nanosheets: Membrane Damage, Metabolic Inactivation, and Oxidative Stress, ACS Applied Bio Materials **2**, 2738-55 (2019).

[50] Kozbial, A., Gong, X., Liu, H., Li, L., Understanding the Intrinsic Water Wettability of Molybdenum Disulfide (MoS2), Langmuir **31**, 8429-35 (2015).